Effects of Imperfect Grooves in Full-Floating Ring Bearings on Dynamics of a Turbocharger Rotor

Luboš SMOLÍK

*University of West Bohemia, Univerzitní 2732/8, 301 00
Plzeň, Czech Republic, carlist@ntis.zcu.cz*

Pavel POLACH

*Research and Testing Institute Plzeň, Tylova 1581/46,
Plzeň, Czech Republic, polach@vzuplzen.cz*

Michal HAJŽMAN

*University of West Bohemia, Univerzitní 2732/8, 301 00
Plzeň, Czech Republic, mhajzman@kme.zcu.cz*

Abstract

Full-floating ring bearings cause nonlinear vibrations of turbocharger rotors, and they have higher hydrodynamic power losses in comparison with rolling element bearings. Both issues can be improved if several shallow axial grooves are machined in the inner surface of the floating ring. The grooves are usually not manufactured precisely in order to keep production costs as low as possible. This work investigates the role of the machining errors on the dynamics of the turbocharger rotor. More specifically, the effects of the precisely-machined grooves on the dynamics of the system are explained. Then the influence of the uncertainties on both vibrations and hydrodynamic power losses in the bearings is investigated.

Keywords: Rotor, dynamics, uncertainty, bearings

1. Introduction

Rotors of turbochargers are supported in full-floating ring bearings (FFRB) in most applications because these bearings are inexpensive and are not prone to the fatigue damage, unlike rolling element bearings. However, due to their design with two oil films, FFRBs cause nonlinear vibrations, are prone to instability and have high power losses. Both dynamics and tribology of the bearing can be improved if several shallow axial grooves are machined in the inner surface of the floating ring. The grooves are not usually manufactured precisely in order to keep production costs as low as possible. Engineering tolerances can be even of the same order as the bearing clearance.

Scientific literature deals with the dimensional uncertainty in the journal bearings only occasionally. In these cases, the attention is mainly paid to the bearing behaviour, not to the rotor behaviour. Maharshi et al. [5] investigated a stochastic behaviour of the journal bearing including the effect of random variabilities in eccentricity and surface roughness. He developed the Monte Carlo simulation algorithm for quantifying bearing stochastic characteristics. Turaga et al. [10] solved the Reynolds equation for finite hydrodynamic bearings with rough surfaces using the stochastic finite element method.

Some literature is focused on journal bearings with axial grooves of fixed dimensions and their influences on rotor dynamics. Nowald et al. [7] investigate the influence of axial grooves in the FFRBs on oscillations of turbocharger rotors. Zhang et al. [11] extended Nowald's work and described the effects of circumferential and axial grooves on the oscillations of the FFRBs supported turbocharger rotor. Eling et al. [12] demonstrated that a multilobe FFRB could be employed to reduce vibrations and the cost of higher friction losses in the bearings. A more significant amount of literature is focused on journal bearings with axial grooves of fixed dimensions without the investigation of the rotor dynamic behaviour; see e.g. [1–4] or [6].

This paper deals with the analysis of dynamics of the turbocharger rotor supported on the FFRBs with shallow axial grooves of uncertain dimensions. First, the effects of a modified groove layout on the dynamics of the system are explained. Then the influence of the dimensional uncertainties on both vibrations and hydrodynamic power losses in the bearings is investigated. For this purpose, a robust numerical approach is used: motions of rotating bodies are described employing a multi-body system formalism and forces acting in the bearings are calculated with the finite-element model, which considers some thermal effects.

2. Equations of Motion for a Turbocharger Rotor

In this paper, the motion of the turbocharger rotor and the floating rings is described employing flexible multi-body dynamics. The motion of each flexible body is separated into a global (gross) motion and elastic deformations (vibrations) relative to the floating frame of reference. Governing equations of motion are derived from the Newton-Euler equations in the form of a differential-algebraic system of equations derived in [8]:

$$\mathbf{M}\dot{\mathbf{v}} + \mathbf{D}\mathbf{v} + \mathbf{K}\mathbf{q} = \mathbf{p}^*(\mathbf{s}, \dot{\mathbf{s}}) + \mathbf{f}^j(\mathbf{s}, \mathbf{w}) + \mathbf{f}^e(\mathbf{s}), \tag{1}$$

$$\dot{\mathbf{q}} = \mathbf{v}(t), \tag{2}$$

$$\dot{\mathbf{x}}_B = \mathbf{v}_B(t), \tag{3}$$

$$\boldsymbol{\theta}_B^T \boldsymbol{\theta}_B = 1, \tag{4}$$

$$2\mathbf{S}(\boldsymbol{\theta}_B)\dot{\boldsymbol{\theta}}_B = \boldsymbol{\Omega}_B, \tag{5}$$

$$\mathbf{r}(\mathbf{q}) = \mathbf{0}, \tag{6}$$

where argument t is omitted for clarity. The system of Equations (1) – (6) is solved with respect to state vector $\mathbf{s} = \left[\mathbf{x}_B^T, \boldsymbol{\theta}_B^T, \dot{\mathbf{x}}_B^T, \boldsymbol{\Omega}_B^T, \mathbf{q}^T, \dot{\mathbf{q}}^T\right]^T$ where $\mathbf{x}_B$ and $\boldsymbol{\theta}_B$ describe position and orientation of the body, respectively. Equation (5) defines the relation between angular velocities $\boldsymbol{\Omega}_B$ and the orientation, which is given by four Euler parameters. Vector $\mathbf{q}$ contains general coordinates that characterize elastic deformations of the body. $\mathbf{M}$, $\mathbf{D}$, $\mathbf{K}$ are constant matrices of mass, damping and stiffness, respectively. Vector $\mathbf{p}^*$ contains nonlinear terms resulting from the global motion, vectors $\mathbf{f}^j$, $\mathbf{f}^e$ incorporate forces resulting from joint constraints and external loading, respectively. Vector $\mathbf{w}$ holds state vectors of all bodies that are connected by joints. All terms are described in detail in reference [8]. Equations (2) and (3) are introduced in order to reduce the order of differential equations,

Equation (4) is the normalization condition for the Euler parameters and finally, Equation (6) ensures that the global motion and the elastic deformations are separated uniquely [8].

We assume that there are no contacts between individual bodies in the FFRBs. Therefore, forces transmitted in the vertical and the horizontal direction can be evaluated as integrals of hydrodynamic pressure p over the outer bearing surface. Furthermore, torque T_{hd}, which results from hydrodynamic friction, acts in each oil film. The total torque acting on the inner bearing surface is

$$T_{hd} = -\int\limits_{(x)} \int\limits_{(s)} \theta \left[\frac{h}{2} \frac{\partial p}{\partial s} + (u_{in} - u_{out})\frac{\mu}{h} \right] ds \, dx, \tag{7}$$

where s, x are the circumferential and the axial coordinates expressed in the global coordinate system, respectively, $\theta = \theta(s, x, t)$ is the percentage of lubricant in the bearing gap, $h = h(s, x, t)$ is the bearing gap, $\mu = \mu(s, x, t)$ is the dynamic viscosity of a lubricant and u_{in}, u_{out} are the velocities of the inner and outer surfaces, respectively.

The distribution of hydrodynamic pressure $p = p(s, x, t)$ is governed by the Reynolds equation. If we assume that the lubricant is an incompressible Newtonian fluid, the lubricant film is thin, the flow in the film is laminar, and both inner and outer bearing surfaces are smooth, the pressure distribution is given as follows [8]

$$\frac{\partial}{\partial s}\left(\frac{\theta h^3}{12 \mu} \frac{\partial p}{\partial s} \right) + \frac{\partial}{\partial x}\left(\frac{\theta h^3}{12 \mu} \frac{\partial p}{\partial x} \right) = \frac{u_{in} + u_{out}}{2} \frac{\partial(\theta h)}{\partial s} + \frac{\partial(\theta h)}{\partial t}, \tag{8}$$

where, which is usually specified as an initial condition. Equation (8) is solved for variable p. If p is lower than p_{cav} in any part of the film, cavitation occurs and the following condition is applied

$$\forall p : p < p_{sat} \Rightarrow p = p_{sat}. \tag{9}$$

Equation (8) is then solved for variable θ in the cavitated areas of the film. In addition to cavitation, pressure losses in feed holes, which interconnect the outer film with the inner film, are also assumed. If the continuity equation holds and friction losses in the feed hole are neglected, the relation between pressure p_o at the outer side of the feed hole and pressure p_i at the inner side of the feed hole reads

$$p_o = p_i + \rho \left[\ddot{\mathbf{x}}_r^T (\mathbf{x}_i - \mathbf{x}_o) - \frac{(\mathbf{\Omega}_r \times \mathbf{x}_i)^2 - (\mathbf{\Omega}_r \times \mathbf{x}_o)^2}{2} + \dot{\mathbf{\Omega}}_r^T(\mathbf{x}_o \times \mathbf{x}_i) \right], \tag{10}$$

where vectors $\mathbf{x}_r$, $\mathbf{x}_i$, $\mathbf{x}_o$ specify positions of the floating ring, the inner side of the feed hole and the outer side of the feed hole, respectively, and vector $\mathbf{\Omega}_r$ holds the angular velocity of the floating ring. More details are given in reference [9].

3. Parameters of the Analyzed Turbocharger

A multi-body model of the turbocharger rotor is depicted in Figure 1. The rotor is composed of a flexible shaft and several rigid bodies whose parameters are shown in Figure 1 and Table 1, respectively. Mass is concentrated into 26 nodes which are linked with the massless Timoshenko beams. Shaft mass and stiffness are calculated using the following material and structural properties: Young modulus $E = 205$ GPa, Poisson's ratio

$v = 0.29$, density $\rho = 7850$ kg m^{-3}. Damping is considered to be proportional to a linear combination of mass and stiffness and it is calculated using Rayleigh damping coefficients $\alpha = 52.4$ s and $\beta = 1.06 \cdot 10^{-6}$ s^{-1}.

The rotor speed is regulated by a controller, which is connected to the rotor by means of a rotational coupling of stiffness $k_r = 100$ N m rad^{-1} and damping $d_r = 1$ N m s rad^{-1}.

External forces except gravity ($g = 9.81$m s^{-2}) are neglected. The rotor is supported by a linear spring/damper of stiffness $k_a = 1.00 \cdot 10^{-6}$ N m^{-1} and damping $d_a = 1.00 \cdot 10^{3}$ N s m^{-1} axially, and by two full-floating ring bearings radially. Nominal dimensions of the bearings are given in Table 2 and detailed geometry is shown in Figure 2a. Axial grooves in the inner film may be difficult to machine precisely and their dimensions are considered to be uncertain. Geometry of the axial grooves is characterized by 60 pairs of mutually independent random variables (groove depth and arc) which are evenly distributed. The exact values of the random variables used for simulations are introduced in Figure 2b.

We assume that operating clearances differ from nominal clearances because dimensions are subject to change due to thermal effects. In this work, the operating clearances are estimated using the linear thermal expansion analysis. Boundary conditions used in the thermal analysis were obtained using the CFD simulation and are specified in Table 3. Coefficients of thermal expansion were considered as follows: steel (shaft) $9.00 \cdot 10^{-6}$ K^{-1}, bronze (floating rings) $1.10 \cdot 10^{-5}$ K^{-1}, and cast iron (bearing housing) $2.04 \cdot 10^{-5}$ K^{-1}.
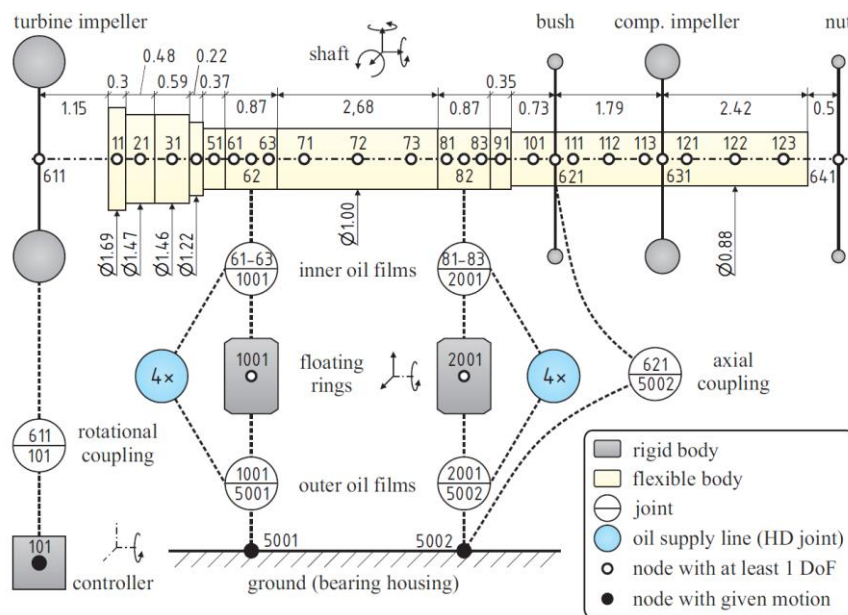

Figure 1. Schematic representation of the analyzed turbocharger. Depicted lengths and diameters are dimensionless; dimensionless length 1 corresponds to ca. 8.5 mm.
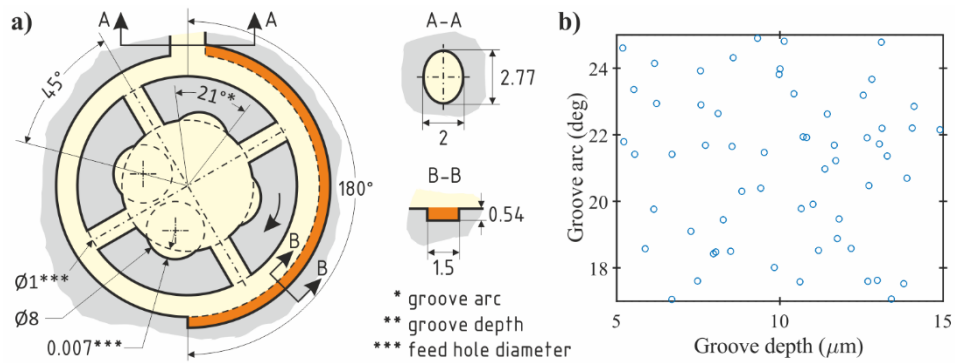
Figure 2. (a) Dimensioned drawing of the floating ring bearing, dimensions are in mm; (b) distribution of random variables.

Table 1. Parameters of rigid bodies including mass *m*, principal moments of inertia about the axis of rotation I_0 and about the transversal axis *I*, and static unbalance U_{st}

Body	Node	m (kg)	I_0 (kg·m²)	I (kg·m²)	U_{st} (g·mm)
turbine wheel	611	$1.42 \cdot 10^{-1}$	$2.38 \cdot 10^{-5}$	$1.96 \cdot 10^{-5}$	$5.40 \cdot 10^{-2}$
distance bush	621	$7.72 \cdot 10^{-3}$	$2.62 \cdot 10^{-7}$	$2.99 \cdot 10^{-7}$	–
compressor impeller	631	$2.80 \cdot 10^{-2}$	$1.95 \cdot 10^{-5}$	$1.33 \cdot 10^{-5}$	$5.40 \cdot 10^{-2}$
nut	641	$4.28 \cdot 10^{-3}$	$8.30 \cdot 10^{-8}$	$7.50 \cdot 10^{-8}$	–
floating ring	–	$5.83 \cdot 10^{-3}$	$1.84 \cdot 10^{-7}$	$1.37 \cdot 10^{-7}$	–

Table 2. Nominal parameters of radial bearings, diameter and length are dimensionless; dimensionless length 1 corresponds to ca. 8.5 mm

Film	Diameter (-)	Length (-)	Clearance (m)	Lubricant	Mesh size
turbine / inner	1.00	0.87	$1.50 \cdot 10^{-5}$	10W-30	121 × 21
turbine / outer	1.54	0.99	$3.25 \cdot 10^{-5}$	10W-30	121 × 21
comp. / inner	1.00	0.87	$1.50 \cdot 10^{-5}$	10W-30	121 × 21
comp. / outer	1.54	0.99	$3.25 \cdot 10^{-5}$	10W-30	121 × 21

Table 3. Temperatures used for the calculation of the viscosity and operating clearances

Side	Speed (rpm)	Shaft (°C)	Inner film (°C)	Outer film (°C)	Housing (°C)
turbine	50000	145	114	105	160
	150000	145	128	108	160
comp.	50000	90	105	90	120
	150000	90	115	95	120

4. Results

In this section, we present the results of the nonlinear steady-state response analysis. The response is obtained at constant speeds of the controller by time-integration of the system of Equations (1) – (6). The total length of the simulation is set so that at least 0.15 s of the response remains after transient response to initial conditions is omitted. The remaining response roughly approximates limit cycle response.

First, we compare the steady-state response of the rotor supported on the mass-produced bearings and on the modified bearings whose layout is shown in Figure 2. The dimensions and clearances of both bearing layouts are identical. The mass-produced bearings have no axial grooves, and the circumferential groove in the outer film is located on the surface of the floating ring rather than bearing housing. The response is simulated at constant rotor speeds which are given by sequence {50, 60, …, 150} krpm. The nominal operating speed of the analysed turbocharger rotor is ca. 130 krpm and it is given by the outer diameter of the compressor impeller.

Figure 3 shows that sub-synchronous vibrations dominate the response in both cases. These vibrations denoted *sub1* and *sub2* in Figures 3c and 3d result from the instability of the outer and the inner film, respectively. A comprehensive theory on the sub-synchronous vibrations can be found in [13] and [14]. The modified bearings attenuate
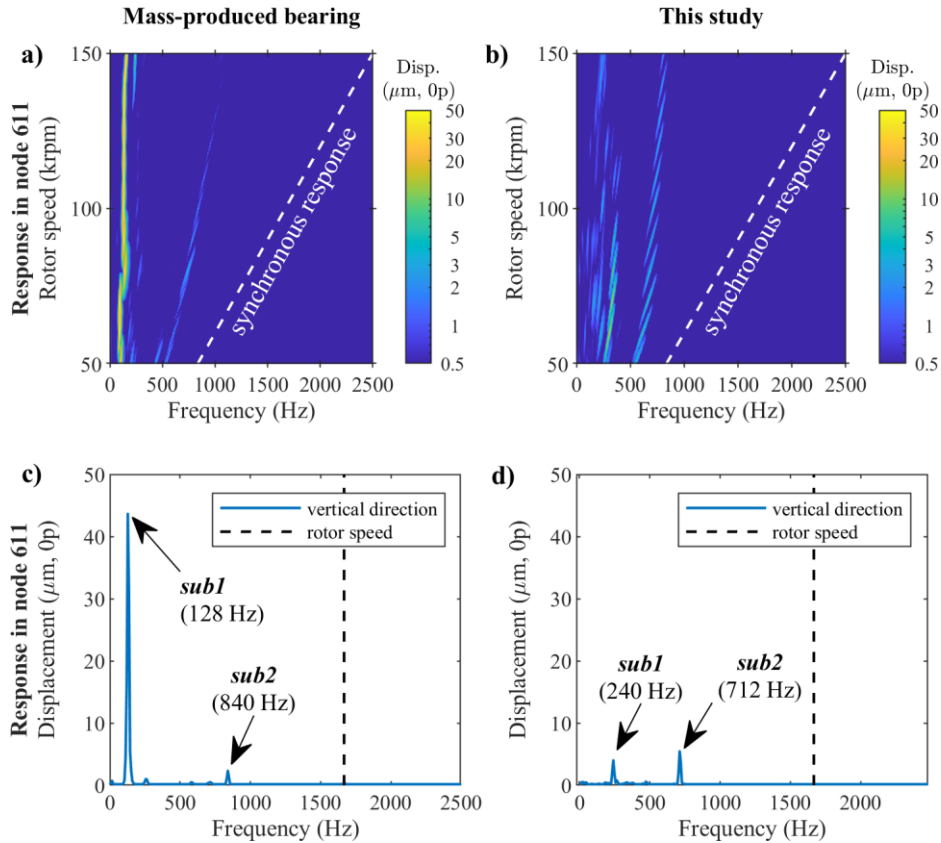
Figure 3. (a, b) FFT of the **steady-state response** at speeds {50; 60; … 150} krpm and (c, d) FFT of the steady-state response at 100 krpm

the magnitude of *sub1* approximately by one order. The attenuation is especially significant at high rotor speeds. Moreover, the modified layout causes a change in the frequency of both *sub1* and *sub2*.

Next, we perform simulations with randomly generated groove depths and arcs. The response is obtained at two rotor speeds – 60 krpm and operating speed 130 krpm. Figure 4 presents some results of these simulations in the form of contour diagrams. Note that several simulations with the grooves deeper than 14 μm did not converge due to the synchronisation of *sub1* with *sub2*, which results in high vibrations and contacts (rubbing) in the inner film of the compressor bearing.

Figures 4a and 4b depict the magnitude and the frequency of *sub2*. Both depend on the ratio between the groove depths and arc at rotor speed 60 krpm. At rotor speed 130 krpm, they depend predominantly at the groove depth. *Sub1* is not analysed here because it splits into two or three components for some values of the random variables. These components result from intermodulation distortion, which is present due to the high nonlinearity of the

system. In this case, the fundamental component *sub1* is rather challenging to identify algorithmically and therefore it is omitted here.

Figures 4c – 4f show maximum relative eccentricity in the inner and outer films – further inner and outer eccentricity, respectively – of the turbine bearing. The maximum relative eccentricity is the percentage of the bearing clearance, which is depleted due to vibrations. The inner eccentricity depends on the ratio between the groove depths and arc at rotor speed 60 krpm. At rotor speed 130 krpm, both eccentricities depend predominantly at the groove depth. The situation is complicated in the case of the outer eccentricity at rotor speed 60 krpm where high values are also reached if the groove depth is maximal and the groove arc is minimal, see Figure 4e.

Finally, Figures 4g and 4h depict mean power loss in the turbine bearing due to hydrodynamic friction. In contrast to the previous results, the power loss tends to be lower when the groove is deeper. Moreover, the power loss is higher when the groove arc is smaller. The relationship, however, is not linear as can be seen in Figure 4h, where the minimum power loss is reached when the groove depth is ca. 10 μm and the groove arc is ca. 24 deg.

The results discussed above are represented by matrices of plots in Figures 5 – 8. Each matrix of plots shows histograms of random variables or outputs on the main diagonal and correlations among pairs of these parameters below the main diagonal. The outputs are represented by the magnitude and frequency of *sub2*, maximum relative eccentricities, the mean power loss and the ring speed ratio, which is defined as the floating ring speed divided by the rotor speed.

As suggested above, many output parameters are almost linearly proportional to the groove depth. On the other hand, the groove arc plays only a minor role in terms of the linear correlation. The diagrams also reveal some exciting relations. First, the inner eccentricity is almost colinear with the outer eccentricity in the compressor bearing at rotor speed 130 krpm, see Figure 8. This phenomenon occurs due to the synchronisation of whirl frequencies. Interestingly, the friction loss in many cases does not correlate with the vibration magnitudes, see Figures 5 – 7. The correlation between the friction loss and the vibration magnitudes is substantial only if the whirl frequencies are synchronised. Moreover, the frequency of *sub2* in many cases correlates with the friction losses.
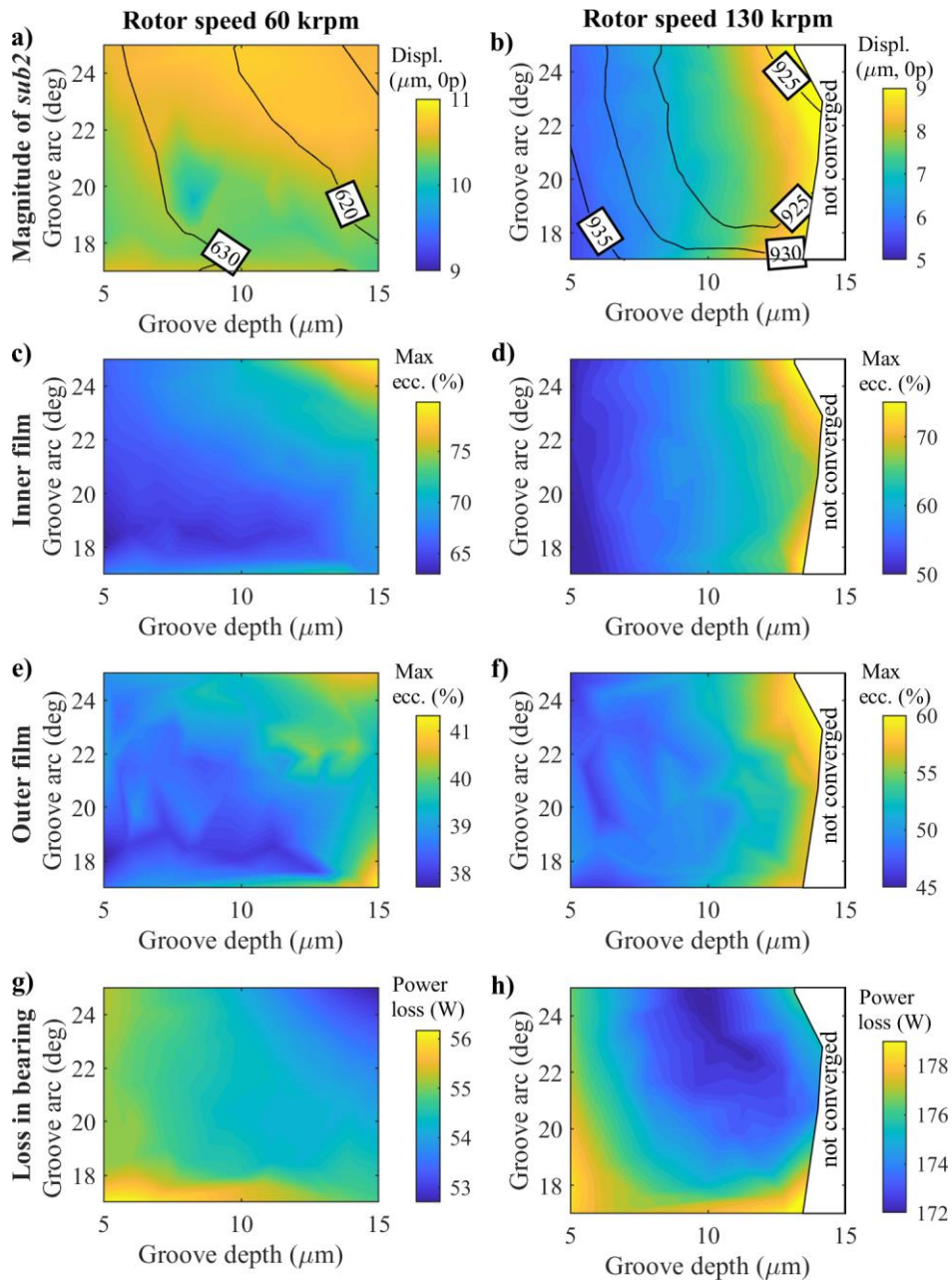
Figure 4. Relationships of various output parameters **in the turbine bearing**
on the groove depth and arc; labels shown in Figures 4a and 4b represents
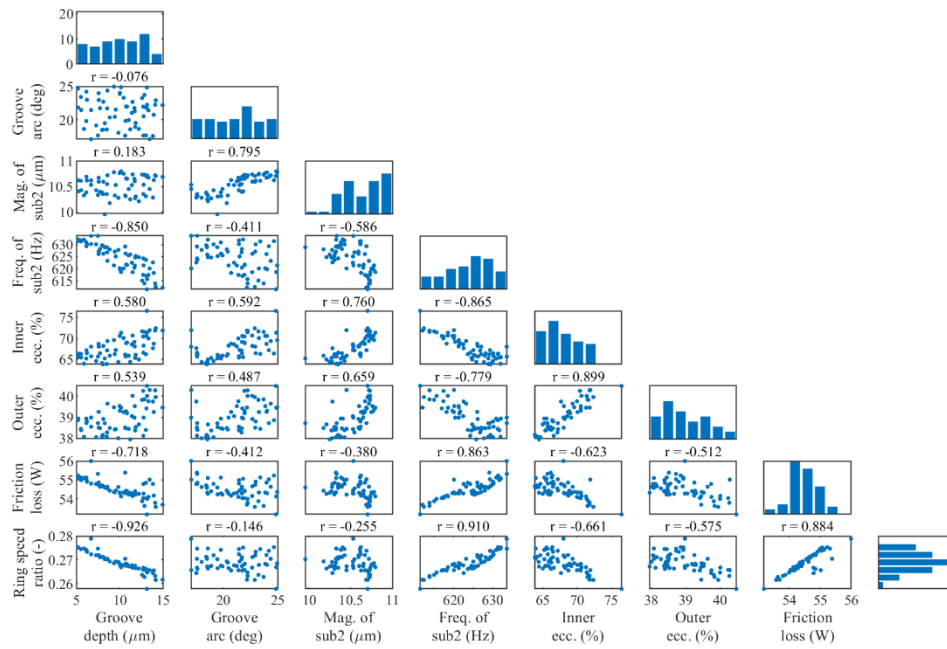the frequency of *sub2* component

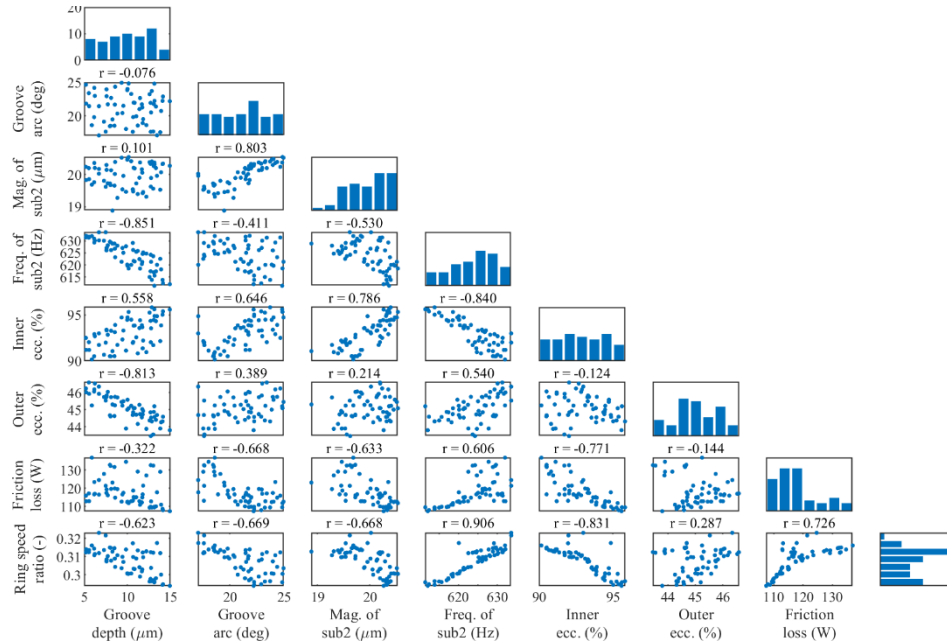Figure 5. Correlation matrix for **the turbine bearing** at rotor speed 60 krpm

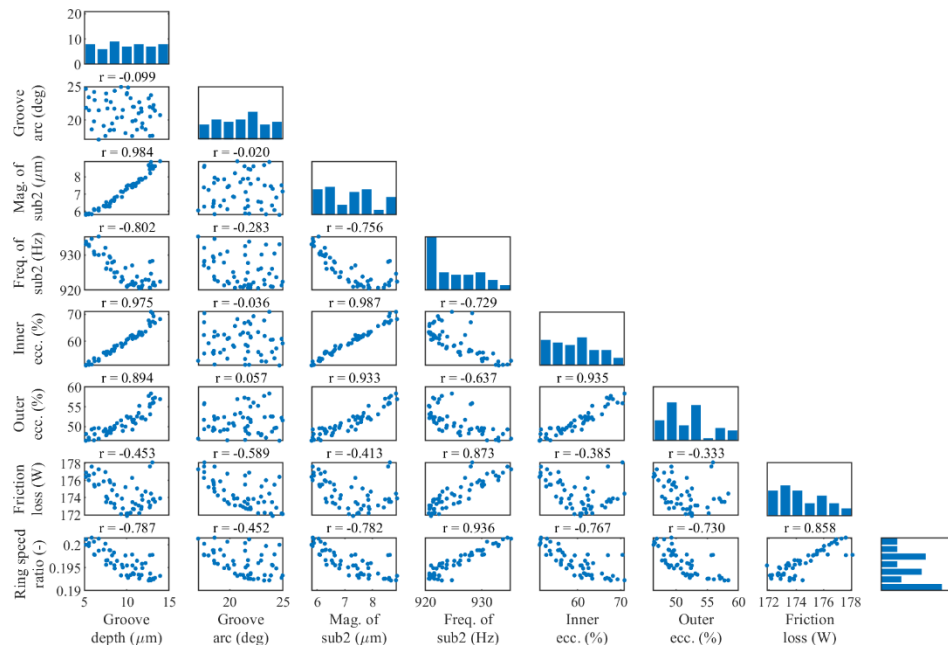Figure 6. Correlation matrix for **the compressor bearing** at rotor speed 60 krpm

Figure 7. Correlation matrix for **the turbine bearing** at rotor speed 130 krpm
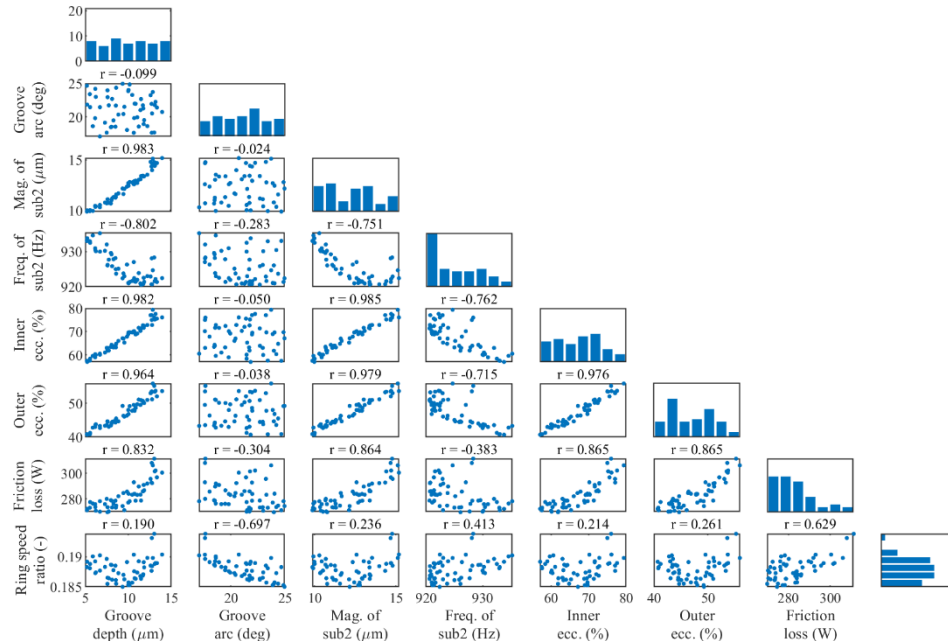

Figure 8. Correlation matrix for **the compressor bearing** at rotor speed 130 krpm

5. Conclusions

This paper has provided a thorough analysis of the nonlinear steady-state response of a turbocharger rotor supported in full-floating ring bearings with imperfect shallow axial grooves. Imperfect geometry is often resulting from inaccurate manufacturing. In this work, we have generated mutually independent geometric variables (groove depth and arc), and we have performed simulations for each geometric configuration.

The axial grooves with the depth of several micrometres can be used in order to improve the performance of the full-floating ring bearing. More specifically, some combinations of the groove depth and arc can minimise the power losses due to hydrodynamic friction while maintaining a desirable level of vibration. However, the shallow grooves have some unwanted properties. In particular, even small changes of the groove depth can lead to a severe deterioration of the bearing performance – most notably the synchronisation of whirl frequencies in the unstable floating ring bearing at high speeds.

The groove depth plays a more prominent role than the groove arc, and especially vibrations tend to be linearly proportional to it. This linear relationship is strong at high speeds. Further generalisations are difficult to express as there are different relations between the variables and the output parameters at various rotor speeds. We can conclude that if any shallow axial grooves are used, the impact of the machining errors should be evaluated.

However, the presented work is limited because we have assumed that all shallow grooves have the same geometry. This assumption is not a case in real applications as each groove can be manufactured with different geometry. Such a situation might lead to new behaviour which is not discussed here.

Acknowledgments

References

1. S. Chatterton, P. Dang, P. Pennacchi, A. De Luca, F. Flumian, *Experimental evidence of a two/axial groove hydrodynamic journal bearing under severe operation conditions*, Tribol. Int., 109 (2017), 416 – 427.

2. R. Flack, G. Kostrzewsky, L. Barrett, *Experimental and predicted rigid rotor stability threshold of axial groove and three-lobe bearings*, Int. J. Rotating Mach., 8 (2002), 27 – 33.

3. J. Knight, L. Barrett, R. Cronan, *The effects of supply pressure on the operating characteristics of two-axial-groove journal bearings*, ASLE Transactions, 28 (2008), 336 – 342.

4. L. Roy, *Effect of axial groove on steady state and stability characteristics of finite two-lobe hybrid journal bearing*, J. Appl. Mech. Eng., 4 (2014) ID100146, 1 – 7.

5. K. Maharshi, T. Mukhopadhyay, B. Roy, L. Roy, S. Dey, *Stochastic dynamic behaviour of hydrodynamic journal bearings including the effect of surface roughness*, Int. J. Mech. Sci., 142 – 143 (2018) 370 – 383.

6. B. Majumdar, R. Pai, D. Hargreaves, *Analysis of water-lubricated journal bearings with multiple axial grooves*, P. I. Mech. Eng. J-J. Eng., 218 (2004) 135 – 146.

7. G. Nowald, A. Boyaci, R. Schmoll, P. Koutsovasilis, N. Driot, B. Schweizer, *Influence of axial grooves in full-floating-ring bearings on the nonlinear oscillations of turbocharger rotors*, In: SIRM 2015 – 11th International Conference on Vibrations in Rotating Machines, Otto-von-Guericke-Universität, (2015) 1 – 8.

8. G. Offner, *Modelling of condensed flexible bodies considering non-linear inertia effects resulting from gross motions*, P. I. Mech. Eng. K-J. Mul., 225 (2011) 204 – 219.

9. G. Offner, F. Diwoky, C. Schweiger, W. Baier, *Coupled oil film lubricated contact simulation for ices*, P. I. Mech. Eng. J-J. Eng., 227 (2013) 447 – 458.

10. R. Turaga, A. Sekhar, B. Majumdar, *Stochastic FEM analysis of finite hydrodynamic bearings with rough surfaces*, Tribol. T., 40 (1997) 605 – 612.

11. C. Zhang, R. Men, H. He, W. Chen, *Effects of circumferential and axial grooves on the nonlinear oscillations of the full floating ring bearing supported turbocharger rotor*, P. I. Mech. Eng. J-J. Eng., 233 (2018) 741 – 757.

12. R.P.T Eling, R.A.J. van Ostayen, D.J. Rixen, *Multilobe floating ring bearings for automotive turbochargers*. In: P Pennacchi (ed.), Proceedings 9th IFToMM International Conference on Rotor Dynamics, Mechanisms and Machine Science, IFToMM Conference 2014, Milan, Springer, 21 (2015) 821 – 833.

13. B. Schweizer, *Dynamics and stability of turbocharger rotors*, Arch. Appl. Mech., 80 (2010) 1017 – 1043.

14. E. Woschke, C. Daniel, S. Nitzschke, *Excitation mechanisms of non-linear rotor systems with floating ring bearings - simulation and validation*, Int. J. Mech. Sci., 134 (2017) 15 – 27.